Journal of Materials Chemistry A

ROYAL SOCIETY OF CHEMISTRY

PAPER

View Article Online
View Journal | View Issue

Cite this: J. Mater. Chem. A, 2020, 8, 12406

Low temperature methane conversion with perovskite-supported *exo*/*endo*-particles

Kalliopi Kousi, *[a] Dragos Neagu, †*[a] Leonidas Bekris,[a] Eleonora Calì,[b] Gwilherm Kerherve,[b] Evangelos I. Papaioannou, [a] David J. Payne[b] and Ian S. Metcalfe*[a]

Received 19th May 2020
Accepted 9th June 2020

DOI: 10.1039/d0ta05122e

rsc.li/materials-a

Lowering the temperature at which CH_4 is converted to useful products has been long-sought in energy conversion applications. Selective conversion to syngas is additionally desirable. Generally, most of the current CH_4 activation processes operate at temperatures between 600 and 900 °C when non-noble metal systems are used. These temperatures can be even higher for redox processes where a gas phase–solid reaction must occur. Here we employ the endogenous-exsolution concept to create a perovskite oxide with surface and embedded metal nanoparticles able to activate methane at temperatures as low as 450 °C in a cyclic redox process. We achieve this by using a non-noble, Co–Ni-based system with tailored nano- and micro-structure. The materials designed and prepared in this study demonstrate long-term stability and resistance to deactivation mechanisms while still being selective when applied for chemical looping partial oxidation of methane.

Introduction

Methane conversion processes are of great importance and interest because they allow the production of energy and fuels independent without exploitation of crude-oil.[1–3] Currently, the most widely used process is the reforming of methane using oxidative streams. However, due to the highly stable C–H bond, reforming is highly endothermic and usually requires high temperatures (600–900 °C), which in turn can lead to catalyst deactivation by coking or sintering.[4,5] The endothermicity is usually addressed by combusting a significant fraction of the methane. Many efforts have been made to decrease the reaction temperature, but promoting methane conversion under mild/moderate temperature conditions still remains a challenge.[5] Moreover, selectivity to desirable products is usually low and as a result, there is a need for product separation.

One way of addressing the above limitations is by using chemical looping partial oxidation (CLPO) in conjunction with exsolved materials. In CLPO, an oxygen carrier material reacts sequentially and cyclically with the reducing (CH_4) and oxidizing streams (air), such that the two never come in contact (eqn (1) and (2)). This results in reduced need for methane combustion, potentially higher selectivity and removes the need for product separation.[6–9]

$$CH_4 + ABO_3[MO] \rightarrow CO + 2H_2 + ABO_{3-\delta}[M] \quad (1)$$

$$ABO_{3-\delta}[M] + O_2 \rightarrow ABO_3[MO] \quad (2)$$

Exsolved materials are usually perovskites where catalytically active elements are initially incorporated in the perovskite lattice and subsequently released as metallic nanoparticles following a thermal treatment in a reducing atmosphere.[10] Such exsolved nanoparticles are partly embedded in the parent perovskite and thus more stable against agglomeration[11] and coking[12,13] and often more active.[14–16]

We have recently demonstrated that the exsolution concept can be controlled to produce systems with particles on the surface as well as in the bulk, leading to oxygen carrier materials that can selectively convert methane to syngas by chemical looping at 600 °C, much lower than similar chemical lopping processes.[17] To further lower this temperature, one would have to increase the surface reactivity of the material as well as increase the oxygen transport through the bulk. One way of achieving these goals simultaneously would be by incorporating Co in the previously designed systems because Co has been shown to improve oxide-ion transport in perovskites.[18] Furthermore, it has been demonstrated experimentally and computationally that mixed Co–Ni spinel oxides activate methane at much lower temperatures than individual Co or Ni oxides due to the local crystallographic and electronic structure environments.[19–25] Additionally, the surface reactivity and oxygen

[a]School of Engineering, Newcastle University, Newcastle-upon-Tyne NE1 7RU, UK. E-mail: kalliopi.kousi@newcastle.ac.uk; dragos.neagu@strath.ac.uk; ian.metcalfe@newcastle.ac.uk

[b]Department of Materials, Imperial College London, Exhibition Road, London SW7 2AZ, UK

† Current address: Department of Process and Chemical Engineering, University of Strathclyde, Glasgow, G1 1XL, UK.

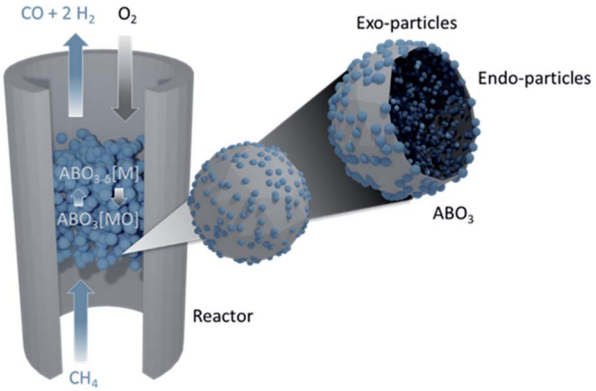

Fig. 1 Schematic representation of chemical looping *via* exsolved particles.

diffusion could be improved by increasing the porosity of the samples.[15,26]

Here we use the design principles outlined above to demonstrate a Co–Ni perovskite oxide system with surface ("*exo*-") and bulk ("*endo*-") nanoparticles that, due to its tailored chemistry and microstructure, can convert methane at temperatures as low as 450 °C (Fig. 1). The materials presented in this study can be used for selective conversion of methane to syngas while being redox stable and coke free over an extended period of time.

Materials and methods

Sample preparation

Perovskite oxide powders were prepared by a modified solid-state synthesis described in detail previously.[13] The as-prepared samples were crushed and sieved to produce powders with particle size between 80–160 μm. To exsolve particles, the samples were reduced at temperature in a controlled atmosphere furnace, under continuous flow of 5% H_2/He (25 mL min^{-1}) with heating and cooling rates of 5 °C min^{-1}. To exsolve particles both on the surface and in the bulk, a temperature of 1000 °C and a dwell of 10 h were employed.

For making the porous materials the use of a pore-former was employed. Glassy carbon was mixed in with the calcined material and then both are pressed in a pellet form before sintering. The sintering temperature was also decreased by 50 °C in order to avoid over-sintering.

For the preparation of 10 wt% Ni/Al_2O_3, as a reference material, a commercial γ-Al_2O_3 powder was used as support (~100 m^2 g^{-1}). Alumina was dispersed in a dilute aqueous solution of nickel nitrate under continuous stirring followed by water evaporation and drying at 90 °C overnight. The dried material was submitted to temperature programmed calcination (10 °C min^{-1}), the final temperature being 500 °C with a dwell of 4 h. After the calcination, the material was sieved to the same size as the exsolved samples, 80–160 μm, and reduced under continuous flow of 5% H_2/He (25 mL min^{-1}) at 900 °C for 4 h with heating and cooling rates of 5 °C min^{-1}.

Oxidation for all the above samples was carried out in air (after the reduction step) at 600 °C for 1 h with heating and cooling rates of 5 °C min^{-1}.

X-ray diffraction

The phase purity and crystal structure of the prepared perovskites was confirmed by room temperature XRD by using a PANalytical X'Pert Pro Multipurpose X-ray diffractometer operated in reflection mode.

High-resolution X-ray diffraction measurements were conducted at the synchrotron ESRF facility (Grenoble, France), at ID22 beam line (MA2914). All the samples were in powder form and a radiation energy of 38 keV (wavelength 0.35448 Å) was used. This energy was chosen as it was as high as practical so as to minimise the absorption by the sample through the relatively large path length of this setup, while staying sufficiently below the lanthanum K-edge of 39 keV. For the room temperature scans, the samples were loaded in 0.5 mm capillaries and scanned at 2θ angles ranging from 0 to 40°, with an average acquisition time of 10 min.

Rietveld refinement analysis was carried out using GSAS II.[27] For the capillary data, background (shifted Chebyshev polynomial, 8–16 terms) unit cell parameters, atomic coordinates, site occupancies, thermal displacement parameters, micro-strain and peak shapes were gradually unlocked and refined. Site occupancies were also constrained to limits given by the cation balance calculations. Background (shifted Chebyshev polynomial, 6–12 terms) unit cell parameters, phase fraction and micro-strain parameters were gradually unlocked and refined. The space groups used are listed in the corresponding figures.

Electron microscopy

High-resolution secondary and backscattered electron images were obtained using a FEI Helios Nanolab 600 scanning electron microscope (SEM).

Samples were analysed by transmission electron microscopy (TEM) using a JEOL JEM-2100F TEM operating at a 200 kV voltage and a FEI Titan operating at a 300 kV voltage equipped with a Cs aberration image corrector. Chemical composition of the samples was determined through energy dispersive X-ray spectroscopy (EDS) operated in scanning-transmission electron microscopy (STEM) mode (EDS 80 mm X-Max detector, Oxford Instruments). Specimens for TEM analysis were prepared by sonication of powder samples in high purity isopropanol subsequently drop-casted on holey carbon film copper grids (3.05 mm diam. 300 mesh, TAAB).

Image analysis. Particle size distributions were calculated based on pixel contrast from SEM micrographs by using a custom made routine in Mathematica, based on a procedure described previously.[14] The Voronoi tessellation was calculated by adjusting a local routine available in Mathematica.

X-ray photoelectron spectroscopy

Spectra were recorded on a Thermo Scientific K-Alpha$^+$ X-ray photoelectron spectrometer operating at 2 × 10^{-9} mbar base

pressure. This system incorporates an Al Kα monochromated X-ray source ($h\nu = 1486.6$ eV) and a 180° double focusing hemispherical analyser with a 2D detector. The X-ray source was operated at 72 W (6 mA, 12 kV) with a spot size of 400 μm^2. All of the high-resolution core level spectra were obtained using a 20 eV pass energy and 0.1 eV step size. A flood gun was used to minimize the sample charging that occurs when exposing an insulated sample to an X-ray beam. The quantitative XPS analysis was performed using the Avantage software. All binding energies were corrected by aligning the C 1s peak of the adventitious carbon to 284.8 eV. The intensity of all spectra was normalised to the area of the Ti $2p_{3/2}$ components. A Shirley background was used for all peak corrections.

Reactor set-up

Two different reactor setups were used, reactor setup 1 and reactor setup 2 described below. For both setups, and depending on the experiment, CH_4, O_2, H_2, CO and CO_2 were continuously monitored (at $m/z = 15$ (CH_4), 32 (O_2), 2 (H_2), 28 (CO) and 44 (CO_2)) by a mass spectrometer (Hiden HAS-301-1291) through a heated capillary line. Calibration gases, CH_4, O_2, H_2, CO and CO_2, all 5% in a balance of He and He as a zero gas were periodically fed into the mass spectrometer (Hiden, QGA) to obtain calibration factors, cracking factors (for CO_2 into CO) and the background current. The largest drift in the calibration signal for a gas was with H_2, which had a relative drift of 3.5% over 24 h. Calibrations with all calibration gases and the zero gas were performed before and after each experiment. One gas is additionally calibrated every 15 cycles and these calibrations were used to correct for any drift observed in the gases. The corrected mass to charge ratio current for all gases was a calibration factor multiplied by the difference between the recorded signal and the background signal, minus any cracking signal from other species on that particular mass to charge ratio channel. The dead time between the outlet of the reactor and the inlet of the mass spectrometer was taken into account in the results presented here.

Stability test set up (reactor set up 1). This reactor setup was used for all chemical looping testing. Briefly, the setup consists of a furnace in a vertical orientation, automated 4-way valves to control the gas composition being fed each time into the reactor, computer-controlled mass flow controllers (SLA5850, Brooks Instrument) that were used to regulate the flow through the system and pressure transducers (PG309-100GV, Omega) to record the system pressure. This set up is described in detail elsewhere.[6] The reactor of the system is a quartz tube with internal diameter of 4 mm and 2 mm wall thickness. The local temperature was recorded with a K-type thermocouple placed in contact with the quartz reactor tube and was increased from RT to the specific experiment's temperature at a rate of 5 °C min^{-1}.

Temperature programmed experiments set up (reactor set up 2). This reactor setup is a simplified version of reactor setup 1, consisting of a quartz tube (with a fixed frit of porosity 3) with an internal diameter of 6 mm with 1.5 mm wall thickness held in a vertical furnace, forming a fixed-bed reactor. Manual mass flow controllers were used to regulate the flow through the bed and a pressure gauge was used to monitor any pressure changes during operation. The temperature was measured in the catalyst bed by using a K-type thermocouple. For all experiments performed in this setup (Fig. 4a and b), the temperature was increased from RT to 750 °C, at a rate of 10 °C min^{-1}, at 1 atm.

Temperature programmed reduction

A known amount of catalyst (approximately 150 mg) was introduced in the reactor and was purged *in situ* with He at room temperature (RT). The temperature was increased from RT to 750 °C at a rate of 5 or 10 °C min^{-1} (depending on the reactor setup used) under a constant flow of reducing gas mixture of 5% CH_4/He (50 mL min^{-1}) at atmospheric pressure, experiment referred to as methane temperature programmed reduction (MTPR). The signals of CH_4, O_2, H_2, CO and CO_2 were continuously monitored by a mass spectrometer (Hiden HAS-301-1291). The MTPR signals were integrated to calculate the total amount of gases produced and consumed.

Temperature programmed oxidation

Temperature programmed oxidation (TPO) was performed to measure the carbon deposition after methane conversion experiments. At the end of each TPR experiment, a weighted amount of the used catalyst (~100 mg) was employed in the experiment. The temperature was increased from RT to 750 °C at a rate of 10 °C min^{-1}, under a constant flow of oxidizing gas mixture of 5% O_2/He (50 mL min^{-1}) at atmospheric pressure. Temperature was kept at 750 °C until the O_2 (CO_2) signal reached the baseline. The signals of O_2, CO and CO_2 were continuously monitored by an MS spectrometer (Hiden HAS-301-1291). For calculating the total amount of carbonaceous deposits, the TPO signals were integrated.

Chemical looping cycling (CL) stability tests

In order to determine the stability of the material, repeated oxidation/reduction cycles were performed in reactor setup 1. The cycling was performed at 1 atm and 550 °C. The reactor was flushed with a helium flow of 30 mL min^{-1} (NTP) prior to commencing testing. The sample was subjected to multi-cycle isothermal reduction under 5% CH_4/He and isothermal oxidation under 5% O_2/He with inlet flow rates of 30 or 50 mL min^{-1}. Reduction and oxidation half cycles were performed for 5 min while inert gas (He) was purged through the reactor for 5 min between each half cycle in order to avoid mixing of the reducing and oxidising gases. The long-term cycling was performed using 300 mg of sample.

Calculations

For the calculation of conversion, selectivity, carbon deposition and capacity, the following values were calculated.

$$N_{CO} = \int_R (y_{CO})_{outlet} n \mathrm{d}t \quad (3)$$

$$N_{CO_2} = \int_R (y_{CO_2})_{outlet} n \mathrm{d}t \quad (4)$$

$$N_C = \int_O (y_{CO_2})_{outlet} n dt + \int_O (y_{CO})_{outlet} n dt \quad (5)$$

$$N_{CH_4} = \int_R (y_{CH_4})_{outlet} n dt \quad (6)$$

where the letter under the integral denotes the reduction step (R for MTPR or half-cycle) or the oxidation step (O for TPO or half-cycle). y_{CO}, y_{CO_2}, y_{CH_4} are the mole fractions of CO, CO_2 and CH_4 at the outlet of the reactor, N_{CO}, N_{CO_2} are the total moles of CO, CO_2, produced, respectively, during the reduction step and N_{CH_4} is the total moles of unreacted CH_4 (measured at the outlet of the reactor). N_C is the total moles of carbon calculated by the mole fractions of CO, CO_2 at the outlet of the reactor during a TPO experiment. n is the total molar flow rate corresponding to each experiment, m is the mass of sample.

Conversion (%) was calculated by the following equation

$$X_{CH_4} = \frac{N_{CO} + N_{CO_2} + N_C}{N_{CO} + N_{CO_2} + N_C + N_{CH_4}} \times 100 \quad (7)$$

Selectivity (%) was calculated by the following equation:

$$S_{CO} = \frac{N_{CO}}{N_{CO} + N_{CO_2} + N_C} \times 100 \quad (8)$$

$$S_{CO_2} = \frac{N_{CO_2}}{N_{CO} + N_{CO_2} + N_C} \times 100 \quad (9)$$

$$S_C = \frac{N_C}{N_{CO} + N_{CO_2} + N_C} \times 100 \quad (10)$$

Carbon deposition (mg_{carbon}/g_{sample}) was calculated by the integration of the curve of CO_2 after TPO experiments. CO was completely absent meaning that the oxidation of the carbon lead only to total combustion products.

$$c = \frac{M_C}{m} N_C \quad (11)$$

M_C is the molar mass of carbon.

Oxygen capacity (mol O/mol of perovskite) was calculated by:

$$\zeta_C = (2N_{CO_2} + N_{CO}) \times \frac{M_P}{m} \quad (12)$$

$$\zeta_X = \frac{f_{Ni}}{M_{Ni}} \times \frac{M_P}{f_P} \quad (13)$$

where ζ_C and ζ_X correspond to the oxygen capacity (expressed as moles of O per moles of perovskite) calculated from MTPR and X-ray diffraction Rietveld refinement, respectively. M_P, M_{Ni} are the molar masses of the perovskite and nickel respectively, m is the sample weight used in the respective experiments, f_{Ni} and f_P are the weight fractions of the respective species calculated from the Rietveld refinement.

The pseudocubic perovskite cell parameter a_p (Å) referred to throughout the paper as "rABO_3 unit cell" was calculated as:

$$a_p = \sqrt[3]{\frac{V}{4}} \quad (14)$$

where V is the volume of the perovskite unit cell calculated from Rietveld refinement.

Relative density d_r was calculated by:

$$d_r = \frac{m_p}{d_t \pi r_p^2 h_p} \times 10^4 \quad (15)$$

where m_p is the mass, r_p is the radius, h_p is the thickness of the sintered pellet and d_t is the theoretical density that each material would have if the pellet was dense.

$$d_t = \frac{M_p}{N_a a_p^3} \quad (16)$$

where M_p is the molar mass of the perovskite, N_a is the Avogadro's number.

Results and discussion

Bulk exsolution in cobalt-based systems

In order to prepare a system with exsolved CoNi particles (Fig. 1), we prepare $La_{0.7}Ce_{0.1}Co_{0.3}Ni_{0.1}Ti_{0.6}O_{3-\delta}$ (LCCNT) by replacing 0.3 out of 0.4 Ni with Co in the perovskite $La_{0.8}Ce_{0.1}Ni_{0.4}Ti_{0.6}O_{3-\delta}$ (LCNT), and adjusting the A-site cation ratio to compensate for the charge difference between Co (+2/+3) and Ni (+2). We synthesize both compositions by a modified solid-state method, sintering them in air at 1400 °C to form the perovskite phase and crush and sieve them to produce powders with perovskite particle size of 80–160 μm. As confirmed by synchrotron X-ray diffraction and Rietveld analysis, the prepared powders are single phase, exhibiting a high degree of crystallinity (illustrated by sharp peaks in X-ray diffraction patterns, Fig. 2b and c).

We then expose the powders to a 5% H_2/He stream at 1000 °C for 10 h in order to exsolve nanoparticles on and under the surface. The microstructure of the resulting samples (Fig. 2a), clearly shows that the integrity of the initial particles was retained and nanoparticles were formed as intended. The particles exsolved in the bulk display key differences in terms of size and population as compared to the ones exsolved on the surface. The bulk particles are much smaller, approximately 10 nm in the bulk *vs.* 40 nm on the surface with the population in the bulk also being significantly higher (compare surface population to cross-section bulk population in Fig. 2a). The high and homogeneous dispersion of exsolved metallic nanoparticles also seemed to cause a decrease in the perovskite host crystallite size and increase in its microstrain by a factor of 2 (Fig. 2b and c).

Quantifying the degree of exsolution was achieved by refining the XRD patterns collected after the reduction of the samples. This revealed that under these pre-treatment conditions, the majority of the metal substituted in the perovskite lattice exsolved, ~0.3 in the case of the LCCNT and ~0.33 for the LCNT out of 0.4 initially substituted. In both cases, this corresponds approximately to 8 out of the 10 wt% of the total metal content initially substituted in the perovskite.

In addition, it seems that after reduction there are some reflections associated with La_2TiO_5 (Fig. 2b and c) that appear in the XRD patterns which seem to have formed due to the

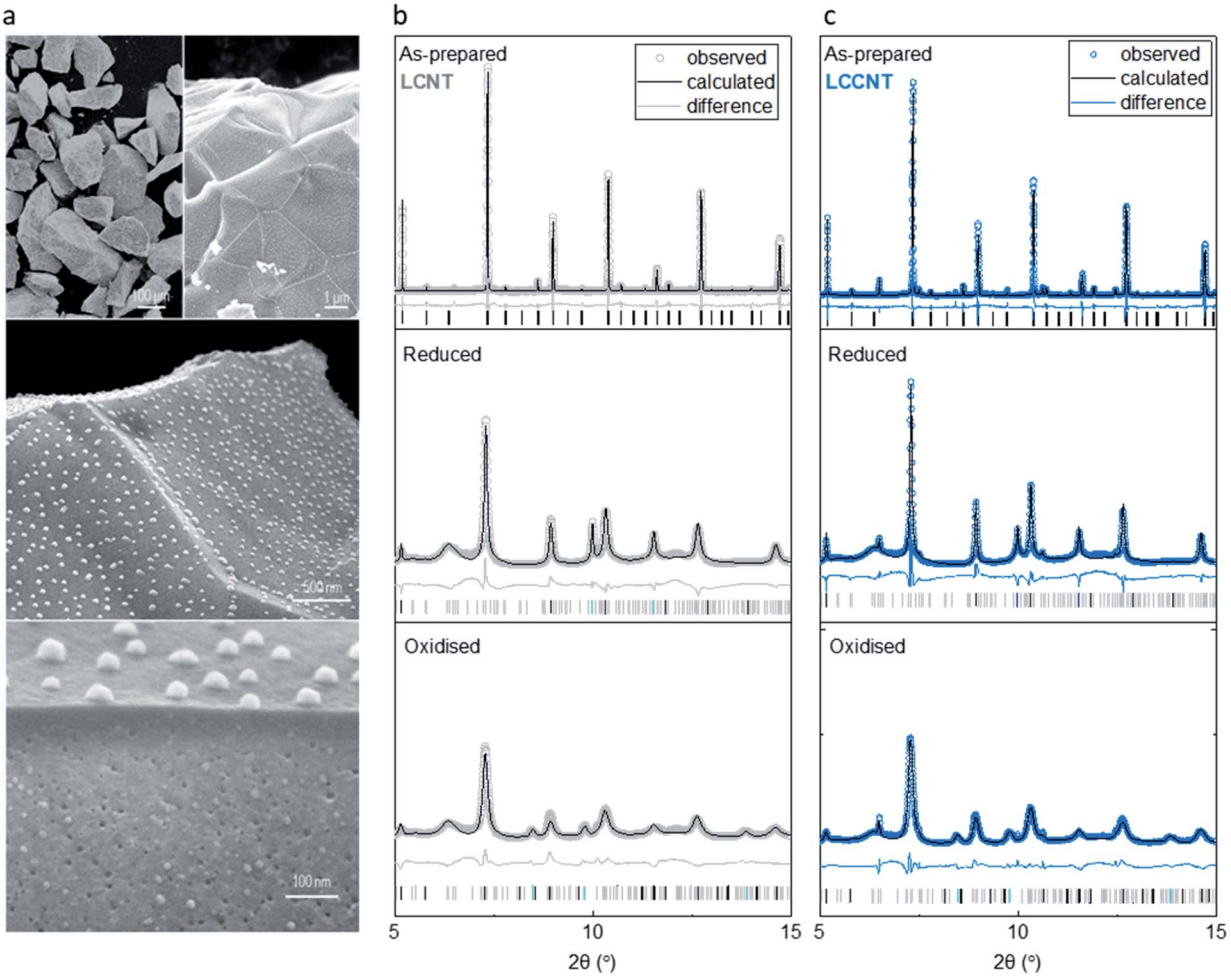

Fig. 2 Microstructure and phase analysis of the samples. (a) SEM micrographs showing, from top to bottom: an overview of the sample and of the surface of the perovskite after exsolution, a cross-section view after exsolution revealing surface and bulk particles. (b and c) Room temperature synchrotron XRD patterns of (b) $La_{0.8}Ce_{0.1}Ni_{0.4}Ti_{0.6}O_{3-\delta}$ and (c) $La_{0.7}Ce_{0.1}Co_{0.3}Ni_{0.1}Ti_{0.6}O_{3-\delta}$ in as-prepared state, after reduction and after oxidation.

extensive degree of exsolution achieved. However, this seems to be a spectator species because it remains unchanged throughout the whole redox process that the material undergoes (Fig. 2b and c). In total, the two compositions are designed such that the extent of exsolution is quite similar for both; this should allow us to deconvolute chemical from microstructural and nanostructural effects that cause any change in reactivity.[21,23,28]

Upon oxidation, all of the metal phase is converted to the metal oxide phase, as indicated by X-ray diffraction and corresponding refinement analysis. The increased peak broadening of the perovskite reveals a further increase in the microstrain inflicted on the host matrix, by a factor of 5 as compared to the reduced state. This is most likely due to the extensive dispersion of the bulk particles and their chemical expansion from metal to metal oxide state. Interestingly, both the Ni sample and CoNi sample adopt the same rock salt crystal structure upon oxidation. This implies that both CO and Ni are present in a +2 oxidation state. If Co would have adopted a higher +3 oxidation state, the presence of a spinel type crystal structure would be present. This would normally be surprising since usually Co metal oxidation in air usually proceeds to a Co^{2+}/Co^{3+} spinel oxide.[29,30] Thus, it seems that here this was inhibited, possibly due to the compressive strain induced onto the particles by the perovskite.

Careful evaluation of the materials' nanostructure *via* TEM confirmed the anchored nature of the surface particles (Fig. 3a) and the existence of both surface and subsurface particles Fig. 3b and c in close proximity. Strikingly, the bulk nanoparticles are highly aligned crystalographically with parent perovskite, forming a distinctive Moire fringe profile. This precise alignment is expected to facilitate oxygen exchange between the embedded metallic particles and the perovskite matrix. In addition, they confirm the high crystallinity of the prepared materials with the FFT patterns indicating the existence of superlattice structures possibly associated with the La_2TiO_5 nanophase (Fig. 3c). EDX mapping of the reduced samples also demonstrates the presence of nanoparticles both on and under the surface, consisting of Ni metal for the LCNT sample (Fig. 3d) and both Co and Ni both homogeneously

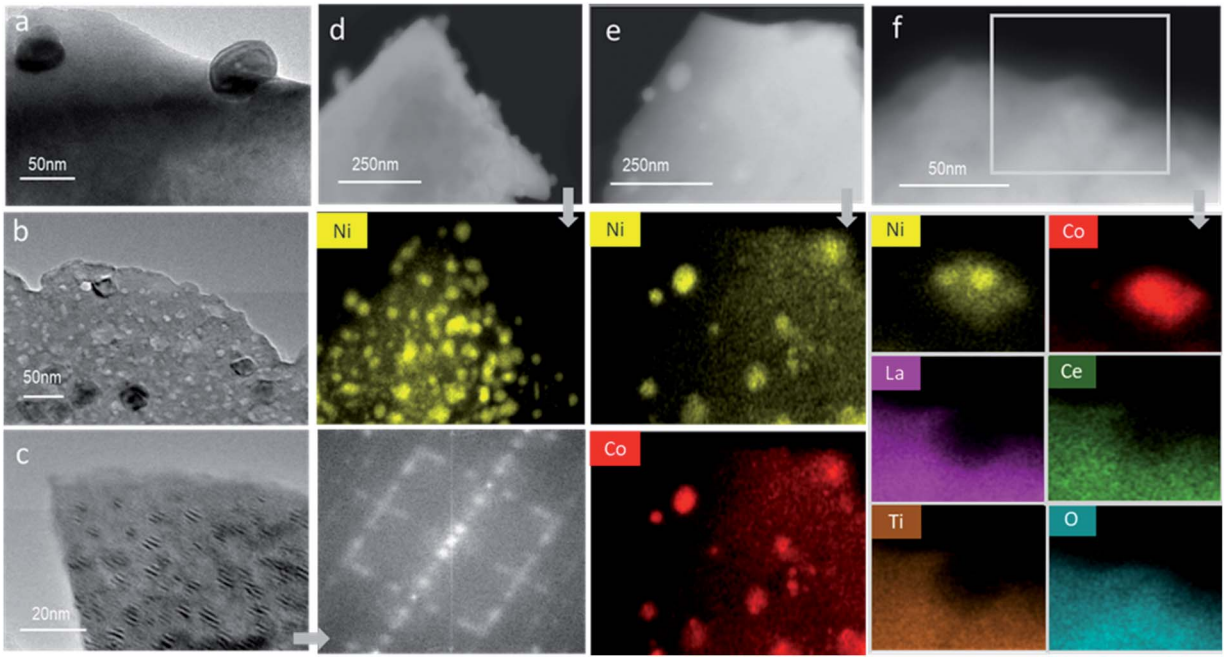

Fig. 3 Nanostructure of the Ni and Co-based samples by TEM. (a) Surface particle embedded in the perovskite matrix. (b) Overview of the perovskite matrix with surface and subsurface particles. (c) Moire fringes characteristic of the samples' morphology and FFT pattern. STEM images and corresponding EDX map of (d). Reduced LCNT sample with mapping indicating the Ni exsolved particles. (e) Reduced LCCNT sample demonstrating the presence of Ni–Co particles. (f) Oxidised LCCNT sample with a bimetallic particle with a both Co and Ni components on the surface and demonstration of the socket in oxidised form by EDX mapping.

mixed throughout each particle for the LCCNT sample (Fig. 3e). For the oxidised LCCNT sample the metal particles largely remain as mixed Co and Ni oxide, although there seems to be a tendency for Ni to segregate at the core of the particle while Co is more homogenously dispersed throughout the nanoparticles. Examination of the EDX images in detail (Fig. 3f) confirms the deeply socketed nature of the exsolved particles at the surface. Note that the EDX maps of La, Ce and Ti form a 'bay'-shaped structure around the particle which contains Co and Ni and O. It is also important to highlight that the embedding of the nanoparticles persists even in their oxidised state, which to the best of our knowledge has yet to be demonstrated so conclusively by using EDX analysis.

Activity enhancement through Co doping

In order to evaluate the ability of the system to activate methane we monitor methane conversion and selectivity as a function of temperature (Fig. 4). We compare, the Co-based system $La_{0.7}Ce_{0.1}Co_{0.3}Ni_{0.1}Ti_{0.6}O_3$ (LCCNT) with the Ni-based counterpart $La_{0.8}Ce_{0.1}Ni_{0.4}Ti_{0.6}O_3$ (LCNT) and a high-surface-area Ni/Al_2O_3 catalyst which has the same amount of active metal, on a weight basis, and is considered as the state-of-the-art catalyst for many hydrocarbon transformations.

The LCCNT displays a CH_4 activation profile characteristic of exsolved materials and very similar to the LCNT counterpart where the perovskite matrix is capable of mediating O transfer between the submerged particles and the surface-activated CH_4 *via* the complex network of strained nano-domains natively produced thought bulk exsolution.[17] Interestingly the CH_4 activation temperature for both Ni-based samples is identical at 580 °C with the exsolved system displaying faster CH_4 conversion and higher resistance to carbon deposition. Additionally, the Co-based sample activates CH_4 in a relatively narrow temperature window, with a sharp consumption peak at 530 °C, followed by a broader peak at 570 °C, selectively yielding syngas with almost a $H_2 : CO_2 : 1$ ratio (with the CO/CO_2 ratio higher than 9 : 1), ideal for methanol production (Fig. 4a). This means that cobalt doping of the LCNT material results in lowering the methane activation temperature by 50 °C while still maintaining high syngas selectivity as compared to the LCNT. Interestingly, the CO_2 feature is only present at the beginning of the cycle and which possibly corresponds to conversion assigned to surface nanoparticles while the rest of the cycle produces pure syngas. This implies that, despite the fact that the water-gas shift reaction would favour the production of CO_2 at these temperatures, what governs the selectivity of the products here is still the kinetics of the gas–solid reaction. Still, throughout the whole experiment, CO and CO_2 production match the CH_4 consumption with a carbon balance that is close to 99% for both perovskites implying almost coke-free testing conditions. The oxygen capacity of the LCCNT system (Fig. 4c) calculated by Rietveld refinement (Fig. 3b, c, 4b and c) and TPR experiment (Fig. 4a and c) is almost identical to the LCNT which would imply that it is not the oxygen capacity of the system that promotes low temperature activation but the synergistic effect between mixed Ni and Co in the particles of the newly designed system.[31] This is not surprising since it has been demonstrated

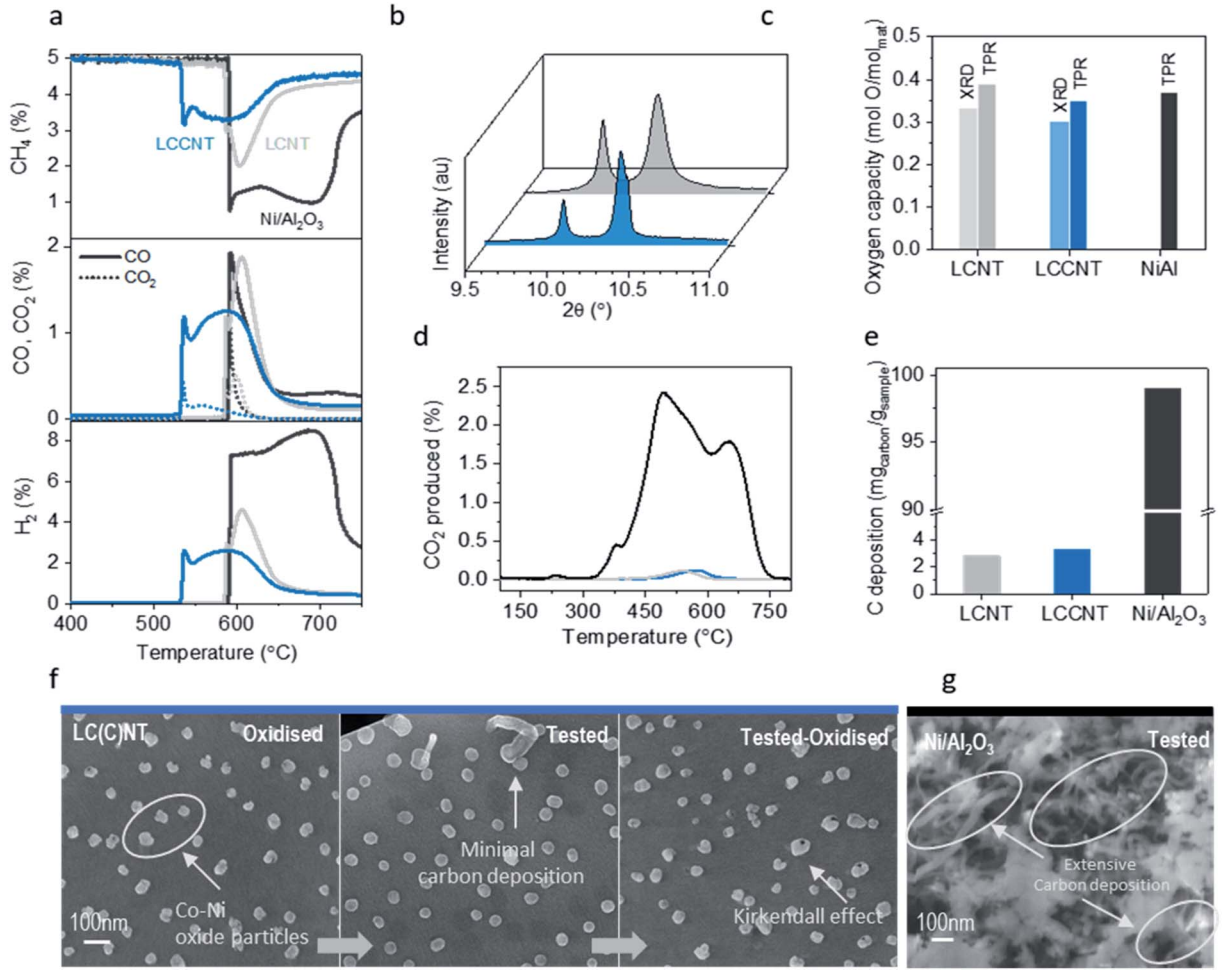

Fig. 4 Comparing activity between Ni and CoNi sample. (a) Conversion of methane to CO, CO_2 and H_2 with temperature for LCNT and LCCNT. (b) X-ray diffraction patterns for the two samples (c). Oxygen capacity calculated by experiment described in (a) and refinement (d). Temperature programmed oxidation experiment after activity testing described in (a). (e) Carbon deposition calculated by integration of the curves in the experiment described in (d). (f) Representative SEM images for both LCNT and LCCNT (hence LC(C)NT) before testing, after testing and after carbon oxidation experiment after testing. (g) Ni/Al_2O_3 sample after testing displaying extensive carbon fibre growth all over the surface of the sample.

before in other catalytic applications that Ni–Co alloys that contain high Co loadings can cause more than one order of magnitude increase in activity for different catalytic processes.[14,22] Interestingly, for the LCCNT system the same overall amount of methane was converted but over a longer period of time, starting at lower temperatures. This indicates that indeed, as mentioned before, the effects presented here are due to the different chemistry of the systems and that Co-based particles are more active, maybe due to the higher oxidation states that cobalt particles can achieve.

Carbon deposition analysis by TPO determined after the above activity testing indicates that indeed the two exsolved samples have similar amount and type of carbon deposition (Fig. 3d) although still minimal in terms of quantity and consistent with the carbon balance (Fig. 4e).

Comparison to the state-of-the-art material for CH_4 conversion, Ni/Al_2O_3 catalyst, shows that the coke deposited on that sample is almost two orders of magnitude higher than the perovskite materials tested in this work (3 *vs.* 100 mg_{carbon}/g_{sample}) over a similar temperature range. The TPO experiment revealed that the carbon on these samples is gassified at different temperatures from 350 to 750 °C, which are typically assigned in the literature to highly crystalline and fibrous carbon profiles (Fig. 4d).[32–34] Specifically, the infiltrated sample has three different kinds (indicated by the three main peaks in the TPO experiment) while only one is present for the exsolved samples (Fig. 4d).

SEM image analysis (Fig. 4f) before and after testing as well as after TPO for both samples shows that all particles retain their position and size after the full redox cycle. The image of the tested sample is characteristic of the negligible amount of carbon deposition on the samples' surface proving that exsolved materials display high tolerance to coking even under harsh reaction conditions. Another interesting point from the SEM images is that oxidised particles are affected by what is known as the Kirkendall effect, generally characteristic of Co nanoparticles.[14] The Kirkendall effect leads to the formation of hollow-core nanoparticles on oxidation due to outward migration of metal ions instead of inward diffusion of oxide ions.

In order to better understand the effect that the substitution of Ni with Co has on the surface of the materials and the particles, we monitor them before and after exsolution, oxidation and testing with X-ray photoelectron spectroscopy (XPS) (Fig. 5). Examination of the XPS data revealed that for the Ni sample (LCNT), the oxidation state and coordination environment of La, Ce and Ti are essentially unchanged throughout the redox processes. La is in its usual +3 oxidation state indicated by a split of 4.6 eV between the main peak and its shake up satellite,[35] while Ti is in its +4 state. Lastly the Ce 3d spectra show only two pairs of peaks corresponding to the Ce 3d $4f^2L$ (u_0 and v_0) and Ce 3d $4f^1L$ (u' and v') which is characteristic of Ce in the +3 oxidation state.[36,37] The small peak observed at binding energy of 916.6 eV corresponds to the Ce $3d_{3/2}$ $4f^0L$ (v'') in the +4 oxidation state. Altogether, this indicates that Ce is predominantly in the +3 oxidation state (Fig. 5a–c). This also suggests

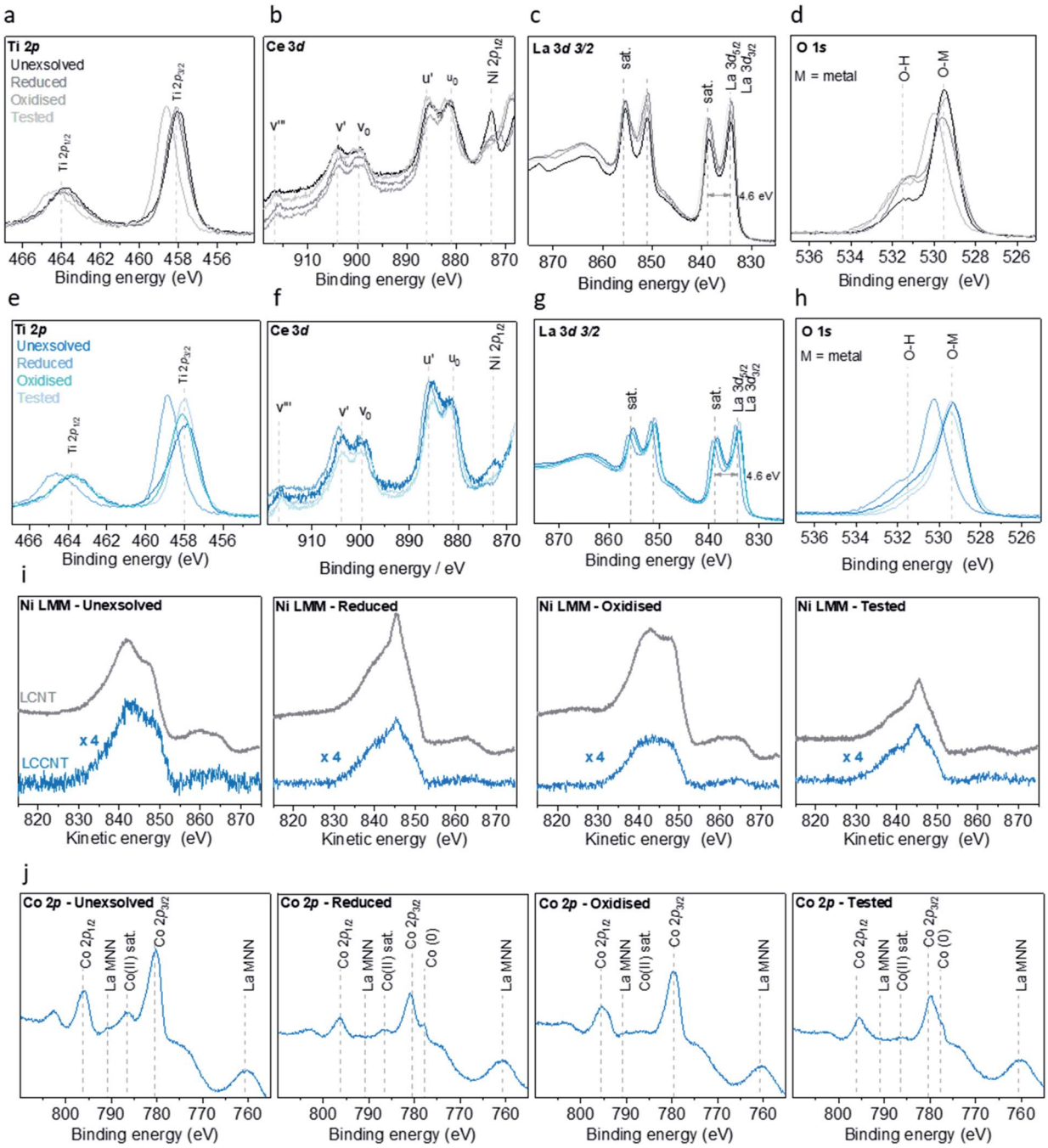

Fig. 5 Surface analysis of the Ni (LCNT) and the Co-based samples (LCCNT). Core level XPS spectra for LCNT of (a) Ti 2p (b) Ce 3d (c) La 3d (d) O 1s. Core level XPS spectra for LCCNT of (e) Ti 2p (f) Ce 3d (g) La 3d (h) O 1s. (i) Core level XPS spectra of Ni $L_3M_{45}M_{45}$ Auger for the unexsolved, reduced, oxidised and tested samples. (j) Core level XPS spectra of Co 2p for the unexsolved, reduced, oxidised and tested LCCNT sample and the Co-based samples (LCCNT).

that these ions most likely have a minimal contribution to the redox processes. Indeed, the most notable change in oxidation state occurs for Ni, as revealed in the Ni $L_3M_{45}M_{45}$ Auger spectra (Fig. 5i). Initially, in the as prepared state, Ni is present in oxide form (NiO) but also to some degree as $Ni(OH)_2$.[38] Upon reduction, and with the formation of exsolved particles, the vast majority of the Ni ions are converted to the metallic state (Fig. 5i). Some Ni^{2+} ions are still likely to remain in the perovskite lattice since not all the Ni that was initially substituted in the perovskite matrix is actually exsolved. Upon oxidation, Ni appears to be present exclusively as NiO and following testing it is again reverted entirely to Ni metal. The Co sample (LCCNT) displays very similar behaviour with respect to the La, Ce, Ti and Ni elements (Fig. 5e–i). Again, La, Ce and Ti appear to be largely redox-inactive, while Ni and Co undergo significant redox changes. In this sample, Ni has the same behaviour as it does in LCNT. Initially Co is predominantly in the +2 oxidation state, converting to the metallic state upon reduction, although some Co^{2+} remains even after prolonged reduction, possibly within the perovskite matrix. Upon oxidation, however, Co is present in a mixed +2 and +3 state (similar to a Co_3O_4-type state). Upon testing and therefore under reducing conditions, Co is converted to metal, again with some remnant Co^{2+} possibly within the perovskite matrix (Fig. 5j). Examination of the O 1s peak (Fig. 5d and h) reveals that the oxygen coordination environment does not change significantly, but additional broadening is also observed at higher binding energy values. These could be due to oxygen in a different environment, such as coordination to Co^{3+} and/or to surface hydroxyl groups. Overall, it appears that the species that are redox active is nickel – cycling between +2 and metallic state, and cobalt – cycling between the slightly higher oxidation states (+2/+3) and metallic state. The fact that the Co reaches slightly higher average oxidation state could account in part for the lower temperature at which they are able to activate methane.

Increasing porosity of Co-based samples

One way of further increasing activity without inflicting chemical changes is by controlling the microstructure. However, for exsolved materials, increasing the porosity of the parent perovskite could affect the exsolution process itself and thus have broader implications on system reactivity. It has been reported before that reducing the perovskite grain size could lead to enhancement of the extent of exsolution,[12,15] since exsolution has been known to draw ions only from a limited depth in the perovskite.[13,39] In turn this could affect the exsolved particle size and population and thus the methane activation temperature, since smaller and more numerous catalytic sites would be available.

We attempt to increase the porosity of the LCCNT perovskite by employing two different approaches. First, we reduce the perovskite sintering temperature by 50 °C, and by XRD (not shown here) we verify that we are still able to get single-phase materials. This way we can avoid over-sintering of the as prepared samples and retain a higher degree of porosity when compared to their higher temperature reduced counterparts. In

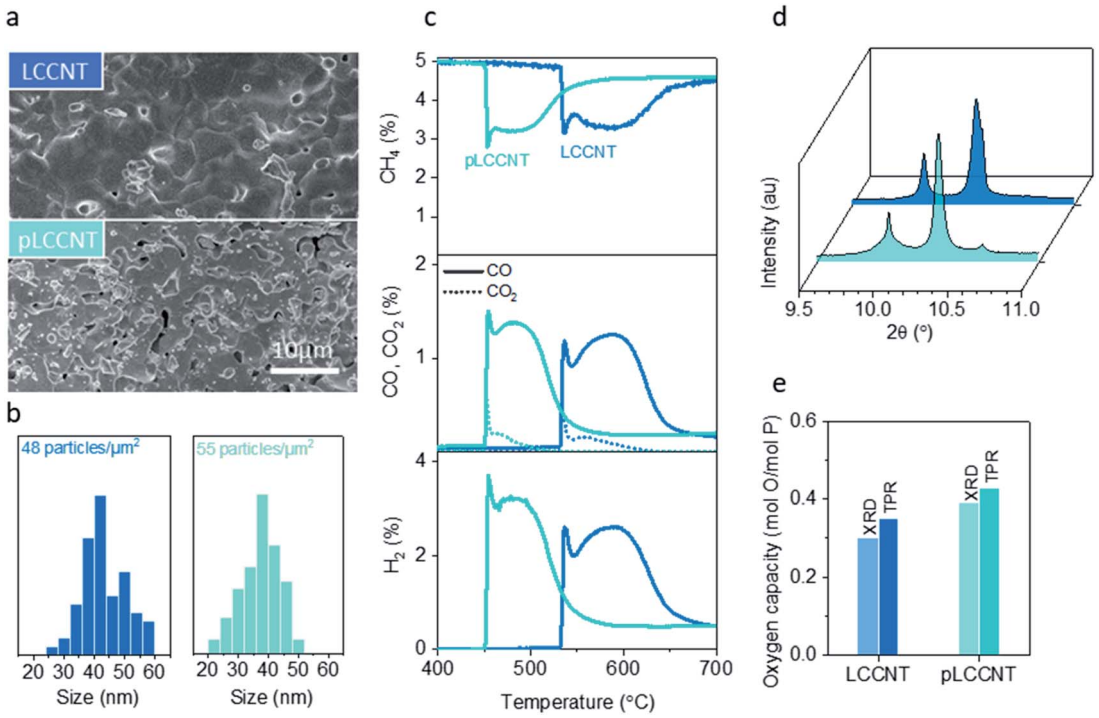

Fig. 6 Increasing porosity in Co-based systems. (a) SEM images of the Co-based perovskite sample before and after porosity enhancement. (b) Particle size analysis of the surface for the samples described in (a). (c) Conversion of methane to CO, CO_2 and H_2 with temperature for the samples described in (a). (d) X-ray diffraction patterns indicating the change in the microstructure and consequent nanostructure of the samples described in (a). (e) Oxygen capacity calculated by TPR experiments (ζ_C) and refinement (ζ_X) of the samples described in (a).

addition, during the sintering phase of the material we employ the use of pore formers. In particular, about 10 wt% of glassy carbon is included when materials are pressed into pellets. The pore former burns under sintering conditions (1350 °C in air) providing us with a material with intrinsic porosity. We measure the relative density (d_r) of the materials after sintering and we find that the density has decreased from 95 to 80% for the newly synthesized material (pLCCNT) (Fig. 6a).

Synchrotron X-ray analysis reveals changes in the nanostructure of the system following the microstructure modification. The peak corresponding to the reduced nickel particles clearly consists of a sharp peak and a second broader one as compared to the original nickel peak corresponding to the LCCNT. This seems to indicate that for the porous materials there is a bimodal distribution of particle size in contrast to the non-modified sample where the particles seem to have a more uniform size (Fig. 6b). However, overall, it is possible that by increasing the porosity of the system we enabled exsolution at the same reduction conditions and that resulted in smaller surface particles which is verified by SEM image particle size analysis. Fig. 6b demonstrates that the size distribution of particles for the pLCCNT is moved to lower values with an average particle size of around 30 nm *vs.* the 40 nm calculated before for LCCNT. In total, despite the fact that the extent of exsolution, and hence the oxygen capacity, is not significantly altered, surface particles in the porous material are smaller and somewhat more numerous which is expected to lower the temperature of the process.[32,40–42]

Indeed, when evaluated under methane as a function of temperature, the two materials seem to have similar oxygen capacity and selectivity (Fig. 6c–e) but the pLCCNT material is able to activate methane at 450 °C which is almost 80 °C lower than the original, less porous, cobalt-based sample. This while still maintaining high selectivity over syngas, with CO/CO_2 ratio higher than 9 : 1 and in addition, carbon deposition is almost non-existent (in both samples) since carbon balance for the whole experiment is more than 99%. This is quite impressive since, as compared to literature data for similar processes, 900 °C are needed in order to get similar conversions and selectivity.[43] Other studies in the literature have been published with a similar scope of lowering the activation temperature of such processes and that have reported similar performance using noble metals to achieve so.[44] Still the results presented here result from a kinetic study and optimization is potentially needed in order for the above to be applied in an industrial process. In addition, the increase in porosity speeded up oxygen exchange with the gas phase since the methane consumption (similar to the reducing half cycle of a chemical looping process) finishes in 15 min, while it takes an additional 3–4 min more for its lower-porosity counterpart to complete the same task. This opens up many possibilities for tailoring exsolved materials not only through their chemistry but also through microstructural control which could be used to indirectly influence their nanostructure and enhance their emergent functionalities.

Application and long-term durability

In order to test the application and long-term stability of the system (pLCCNT), we undertake the chemical looping partial oxidation of CH_4 (CLPO). We test the system under the conditions identified as suitable by the TPR experiments conducted above and by comparing with literature reports of similar

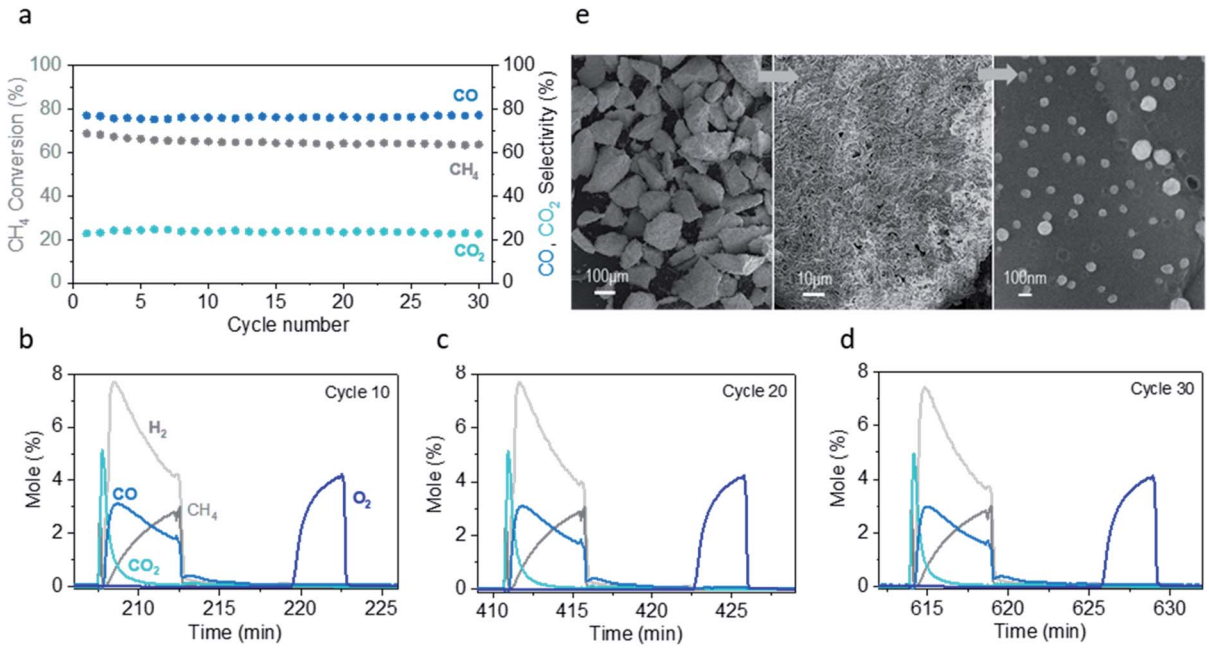

Fig. 7 Stability in Methane partial oxidation to syngas *via* chemical looping. (a) Conversion of CH_4 and selectivity to CO and CO_2 with cycle number. (b) Outlet gas composition over time in the 10th cycle. (c) Outlet gas composition over time in the 20th cycle. (d) Outlet gas composition over time in the 30th cycle. (e) SEM images of the surface after the experiment described in (a).

applications. We therefore use 300 mg of material and operate our system at 550 °C and 30 mL min^{-1} (NTP).

The conversion with the Co sample remains constant at 60% over 30 cycles while the selectivity to CO is stable at 80% (Fig. 7a) (calculated for the duration of each cycle). Usually even the most promising materials in the literature applied for CL show an initial drop in activity and change in the selectivity over the first 10–20 cycles before stabilising (or further decline) or require much higher temperature to achieve similar conversions.[45,46] Here we show that it is possible to have a material that maintains its initial performance over multiple cycles. In addition, there is no carbon deposition present throughout the duration of the experiment (Fig. 7b–d).

After long-term testing, the material shows minimal signs of degradation (Fig. 7e). Microstructural analysis *via* SEM demonstrates no cracks in the material, proof of the mechanical durability of these systems and the nanostructure appears to be almost intact with minimal agglomeration or de-socketing of the particles after 30 cycles (Fig. 7e).

Conclusions

In this work we design and test a perovskite that is capable of exsolving surface and subsurface exsolved Ni–Co particles aiming to lower the temperature at which CH_4 is converted to useful products. We lower the CH_4 activation temperature from 600 °C to 450 °C *via* an *exo*/*endo* particle system while still using base metal systems. We achieve this by doping Ni systems with Co and further tuning the microstructure and nanostructure of the materials.

The materials created have a large fraction of embedded-metal phase which means that the system displays a very large oxygen storage capacity, comparable to that of composites. At the same time, these materials exhibit low carbon deposition and seemingly high coke tolerance if any deposition should occur, consistent with previous reports using exsolved nanoparticles in hydrocarbon environments.[13] Analysis of the samples by TEM and XPS demonstrates that the exsolved particles consist mainly of a mixed Ni–Co oxide which seems to account for the higher activity that the doped samples display. Reducing the grain size of the Co-based system seems to further increase activity by altering surface exsolution, making surface particles smaller and more numerous hence decreasing the CH_4 activation temperature even further.

High oxygen capacity and stability, demonstrated here, while still demonstrating high surface activity, are important for redox cycling applications such as chemical looping, thermochemical solar to fuels conversion or three-way catalysts. These combined with the fact that the endogenous particles are fully accessible to the gas stream while not actually coming in contact with it means that classic deactivation mechanisms such as sulfur and carbon poisoning and sintering could be bypassed leading to highly stable self-assembled nanostructures.

Data availability

The data supporting this publication is available at DOI: 10.25405/data.ncl.9892238.

Conflicts of interest

There are no conflicts to declare.

Acknowledgements

We acknowledge the support of the European Synchrotron Radiation Facility (ESRF) for experiment no. MA-4239. We would like to thank Dr Catherine Dejoie for her valuable help during data acquisition at beamline ID22. We also thank Dr Budhika Mendis and Durham University Microscopy Facility for access. The research leading to these results has received funding from the European Research Council under the European Union's Seventh Framework Programme (FP/2007–2013)/ERC Grant Agreement Number 320725 and from the EPSRC *via* grants EP/P007767/1, EP/P024807/1 and EP/R023921/1.

References

1 B. Wang, S. Albarracín-Suazo, Y. Pagán-Torres and E. Nikolla, *Catal. Today*, 2017, **285**, 147–158.
2 E. V. Kondratenko, T. Peppel, D. Seeburg, V. A. Kondratenko, N. Kalevaru, A. Martin and S. Wohlrab, *Catal. Sci. Technol.*, 2017, **7**, 366–381.
3 N. Agarwal, S. H. Taylor and G. J. Hutchings, in *Frontiers of Green Catalytic Selective Oxidations*, ed. K. P. Bryliakov, Springer Singapore, Singapore, 2019, pp. 37–59.
4 E. D. Goodman, A. A. Latimer, A.-C. Yang, L. Wu, N. Tahsini, F. Abild-Pedersen and M. Cargnello, *ACS Appl. Nano Mater.*, 2018, **1**, 5258–5267.
5 X. Cui, H. Li, Y. Wang, Y. Hu, L. Hua, H. Li, X. Han, Q. Liu, F. Yang, L. He, X. Chen, Q. Li, J. Xiao, D. Deng and X. Bao, *Chem*, 2018, **4**, 1902–1910.
6 I. S. Metcalfe, B. Ray, C. Dejoie, W. Hu, C. de Leeuwe, C. Dueso, F. R. García-García, C.-M. Mak, E. I. Papaioannou, C. R. Thompson and J. S. O. Evans, *Nat. Chem.*, 2019, **11**, 638.
7 J. Huang, W. Liu, W. Hu, I. Metcalfe, Y. Yang and B. Liu, *Appl. Energy*, 2019, **236**, 635–647.
8 K. Svoboda, A. Siewiorek, D. Baxter, J. Rogut and M. Pohořelý, *Energy Convers. Manage.*, 2008, **49**, 221–231.
9 A. J. Carrillo, K. J. Kim, Z. D. Hood, A. H. Bork and J. L. M. Rupp, *ACS Appl. Energy Mater.*, 2020, **3**, 4569–4579.
10 D. Neagu, G. Tsekouras, D. N. Miller, H. Ménard and J. T. S. Irvine, *Nat. Chem.*, 2013, **5**, 916–923.
11 G. Dimitrakopoulos, A. F. Ghoniem and B. Yildiz, *Sustainable Energy Fuels*, 2019, **3**, 2347–2355.
12 S.-K. Otto, K. Kousi, D. Neagu, L. Bekris, J. Janek and I. S. Metcalfe, *ACS Appl. Energy Mater.*, 2019, **2**, 7288–7298.
13 D. Neagu, T.-S. Oh, D. N. Miller, H. Ménard, S. M. Bukhari, S. R. Gamble, R. J. Gorte, J. M. Vohs and J. T. S. Irvine, *Nat. Commun.*, 2015, **6**, 8120.
14 D. Neagu, E. I. Papaioannou, W. K. W. Ramli, D. N. Miller, B. J. Murdoch, H. Ménard, A. Umar, A. J. Barlow, P. J. Cumpson, J. T. S. Irvine and I. S. Metcalfe, *Nat. Commun.*, 2017, **8**, 1855.

15 C. Tang, K. Kousi, D. Neagu, J. Portolés, E. I. Papaioannou and I. S. Metcalfe, *Nanoscale*, 2019, **11**, 16935–16944.
16 V. Kyriakou, D. Neagu, E. I. Papaioannou, I. S. Metcalfe, M. C. M. van de Sanden and M. N. Tsampas, *Appl. Catal., B*, 2019, **258**, 117950.
17 K. Kousi, D. Neagu, L. Bekris, E. I. Papaioannou and I. S. Metcalfe, *Angew. Chem., Int. Ed.*, 2020, **59**, 2510–2519.
18 Z. Shao and S. M. Haile, *Nature*, 2004, **431**, 170–173.
19 F. F. Tao, J. Shan, L. Nguyen, Z. Wang, S. Zhang, L. Zhang, Z. Wu, W. Huang, S. Zeng and P. Hu, *Nat. Commun.*, 2015, **6**, 1–10.
20 J. Horlyck, C. Lawrey, E. C. Lovell, R. Amal and J. Scott, *Chem. Eng. J.*, 2018, **352**, 572–580.
21 L. Xu, F. Wang, M. Chen, J. Zhang, K. Yuan, L. Wang, K. Wu, G. Xu and W. Chen, *ChemCatChem*, 2016, **8**, 2536–2548.
22 T. H. Lim, S. J. Cho, H. S. Yang, M. H. Engelhard and D. H. Kim, *Appl. Catal., A*, 2015, **505**, 62–69.
23 Z. Wu, B. Yang, S. Miao, W. Liu, J. Xie, S. Lee, M. J. Pellin, D. Xiao, D. Su and D. Ma, *ACS Catal.*, 2019, **9**, 2693–2700.
24 D. Zeng, Y. Qiu, S. Zhang, L. Ma, M. Li, D. Cui, J. Zeng and R. Xiao, *Int. J. Hydrogen Energy*, 2019, **44**, 21290–21302.
25 Z. Feng, C. Du, Y. Chen, Y. Lang, Y. Zhao, K. Cho, R. Chen and B. Shan, *Catal. Sci. Technol.*, 2018, **8**, 3785–3794.
26 K. Kousi, D. Neagu and I. S. Metcalfe, *Catalysts*, 2020, **10**, 468.
27 B. H. Toby and R. B. Von Dreele, *J. Appl. Crystallogr.*, 2013, **46**, 544–549.
28 J. Guerrero-Caballero, T. Kane, N. Haidar, L. Jalowiecki-Duhamel and A. Löfberg, *Catal. Today*, 2019, **333**, 251–258.
29 H.-Y. Wang, S.-F. Hung, H.-Y. Chen, T.-S. Chan, H. M. Chen and B. Liu, *J. Am. Chem. Soc.*, 2016, **138**, 36–39.
30 T. Kessler, A. Visintin, M. R. de Chialvo, W. E. Triaca and A. J. Arvia, *J. Electroanal. Chem. Interfacial Electrochem.*, 1989, **261**, 315–329.
31 M. Guo, Z. Cheng, Y. Liu, L. Qin, J. Goetze, J. A. Fan and L.-S. Fan, *Catal. Today*, DOI: 10.1016/j.cattod.2019.06.016.
32 C. Papadopoulou, H. Matralis and X. Verykios, in *Catalysis for Alternative Energy Generation*, ed. L. Guczi and A. Erdôhelyi, Springer New York, New York, NY, 2012, pp. 57–127.
33 M.-S. Fan, A. Z. Abdullah and S. Bhatia, *ChemCatChem*, 2009, **1**, 192–208.
34 L. Chen, Y. Lu, Q. Hong, J. Lin and F. M. Dautzenberg, *Appl. Catal., A*, 2005, **292**, 295–304.
35 M. F. Sunding, K. Hadidi, S. Diplas, O. M. Løvvik, T. E. Norby and A. E. Gunnæs, *J. Electron Spectrosc. Relat. Phenom.*, 2011, **184**, 399–409.
36 A. Kotani, T. Jo and J. C. Parlebas, *Adv. Phys.*, 1988, **37**, 37–85.
37 A. Pfau and K. D. Schierbaum, *Surf. Sci.*, 1994, **321**, 71–80.
38 M. C. Biesinger, L. W. M. Lau, A. R. Gerson and R. S. C. Smart, *Phys. Chem. Chem. Phys.*, 2012, **14**, 2434–2442.
39 D. Neagu, V. Kyriakou, I.-L. Roiban, M. Aouine, C. Tang, A. Caravaca, K. Kousi, I. Schreur-Piet, I. S. Metcalfe, P. Vernoux, M. C. M. van de Sanden and M. N. Tsampas, *ACS Nano*, 2019, **13**, 12996–13005.
40 F. Touahra, R. Chebout, D. Lerari, D. Halliche and K. Bachari, *Energy*, 2019, **171**, 465–474.
41 O. Akbarzadeh, N. A. Mohd Zabidi, Y. Abdul Wahab, N. A. Hamizi, Z. Z. Chowdhury, Z. M. Aljunid Merican, M. Ab Rahman, S. Akhter, M. Shalauddin and M. R. Johan, *Symmetry*, 2019, **11**, 7.
42 T. V. Choudhary and V. R. Choudhary, *Angew. Chem., Int. Ed.*, 2008, **47**, 1828–1847.
43 X. P. Dai, R. J. Li, C. C. Yu and Z. P. Hao, *J. Phys. Chem. B*, 2006, **110**, 22525–22531.
44 V. P. Haribal, X. Wang, R. Dudek, C. Paulus, B. Turk, R. Gupta and F. Li, *Adv. Energy Mater.*, 2019, **9**, 1901963.
45 Y. J. Wong, M. K. Koh, M. Khavarian and A. R. Mohamed, *Int. J. Hydrogen Energy*, 2017, **42**, 28363–28376.
46 T. Li, R. S. Jayathilake, D. D. Taylor and E. E. Rodriguez, *Chem. Commun.*, 2019, **55**, 4929–4932.